



CHALMERS
UNIVERSITY OF TECHNOLOGY

Multiconfigurational Ground State of a Diradicaloid Characterized at the Atomic Scale

Downloaded from: <https://research.chalmers.se>, 2026-06-14 03:48 UTC

Citation for the original published paper (version of record):

Turco, E., Tejerina, L., Catarina, G. et al (2025). Multiconfigurational Ground State of a Diradicaloid Characterized at the Atomic Scale. *Journal of the American Chemical Society*, 147(43).
<http://dx.doi.org/10.1021/jacs.5c13039>

N.B. When citing this work, cite the original published paper.

Multiconfigurational Ground State of a Diradicaloid Characterized at the Atomic Scale

Elia Turco,* Lara Tejerina,# Gonçalo Catarina,# Andres Ortega-Guerrero, Nils Krane, Leo Gross, Michal Juríček, and Shantanu Mishra*



Cite This: *J. Am. Chem. Soc.* 2025, 147, 39616–39622



Read Online

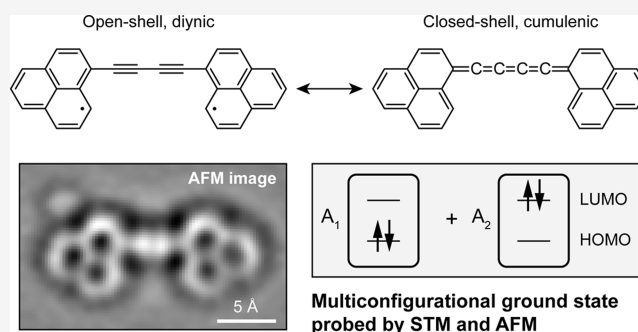
ACCESS |

Metrics & More

Article Recommendations

Supporting Information

ABSTRACT: We report the tip-induced generation and scanning probe characterization of a singlet diradicaloid, consisting of two phenalenyl units connected by an sp -hybridized C_4 chain on an ultrathin insulating NaCl surface. The bond-order contrast along the C_4 chain measured by atomic force microscopy and mapping of charge-state transitions by scanning tunneling microscopy, in conjunction with multiconfigurational calculations, reveal that the molecule exhibits a many-body ground state. Our study experimentally demonstrates the manifestation of strong electronic correlations in the geometric and electronic structures of a single molecule.



INTRODUCTION

Diradicaloids represent an intriguing class of compounds whose reactivity and enigmatic electronic structure have fascinated chemists and physicists for over a century.^{1–3} As intermediates between diradicals and closed-shell molecules, their nature is central to understanding the chemical bond itself. Diradicaloids are represented as resonance hybrids between open- and closed-shell structures, which underscores the ambiguity in defining their electronic structure with theories that do not account for the multiconfigurational nature of electronic wave functions. The small gap between the highest occupied and lowest unoccupied molecular orbitals (HOMO and LUMO) of diradicaloids facilitates the mixing between multiple electronic configurations in the singlet ground state. This multiconfigurational nature is commonly quantified by the diradical index, which can take values between 0 (closed-shell) and 1 (diradical).^{4,5} A well-established correlation between aromatic stabilization and diradical character enables fine-tuning of the electronic and magnetic properties through structural design, making diradicaloids promising candidates for applications in optoelectronics and spintronics.⁶

Driven by progress in synthetic methods and improved characterization techniques, a number of singlet diradicaloids have been studied in recent years, for example, long acenes,^{7–9} periacenes,¹⁰ anthenes,^{11–13} zethrenes,^{14–19} rhombenes,^{20,21} and indenofluorenes.^{22–25} The advent of on-surface chemistry²⁶ has extended the scope of the study of singlet diradicaloids to the atomic scale by means of scanning probe techniques. In this context, it is important to understand how the multiconfigurational ground state of singlet diradicaloids

manifests in terms of the fundamental observables of a molecular system, such as bond order and molecular orbital densities.

In this study, we use atomic force microscopy (AFM) and scanning tunneling microscopy (STM) to generate and study a diradicaloid, **1** ($C_{30}H_{16}$, Figure 1), and elucidate the influence of electronic correlations on the geometric and electronic structures of the molecule. Compound **1** consists of two phenalenyl units (Figure 1a), sp^2 -conjugated polycyclic conjugated hydrocarbons with an $S = 1/2$ (doublet) ground state (S denotes the total spin quantum number), which are connected through their majority sublattice carbon atoms via an sp -hybridized C_4 chain, resulting in an $S = 0$ (singlet) ground state as per Ovchinnikov's rule.^{27,28}

As shown in Figure 1b, compound **1** can be represented as a resonance hybrid of two structures, namely, open- and closed-shell singlets. Importantly, the two resonance structures present different bonding motifs in the C_4 chain, namely, diynic (alternating single and triple bonds) and cumulenic (all double bonds) for the open- and closed-shell structures, respectively. Previously, Hirao et al. studied a derivative of **1** in single-crystalline form.²⁹ From X-ray structural analyses at temperatures between 100 and 250 K, the authors observed a bond-length alternation $b_A - b_B > 0$ at all temperatures (see

Received: July 30, 2025

Revised: October 1, 2025

Accepted: October 13, 2025

Published: October 17, 2025



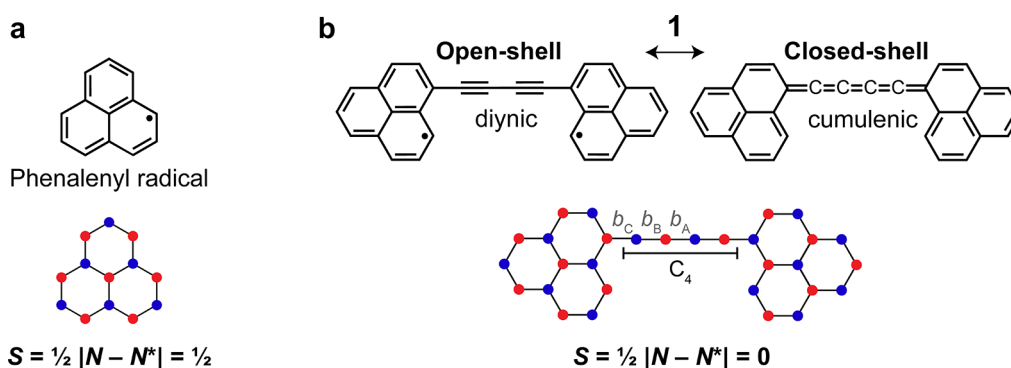


Figure 1. (a,b) Chemical structures and sublattice representations of phenalenyl radical (a) and compound **1** (b). The two sublattices are represented with different colors. N and N^* denote the number of carbon atoms in the two sublattices. For **1**, two possible resonance structures are shown, namely, an open-shell with a diynic C_4 chain, and a closed-shell with a cumulenonic C_4 chain. For the closed-shell resonance structure, the bond orders of b_A , b_B , and b_C should be similar, while for the open-shell resonance structure, b_B should have a higher bond order than b_A and b_C .

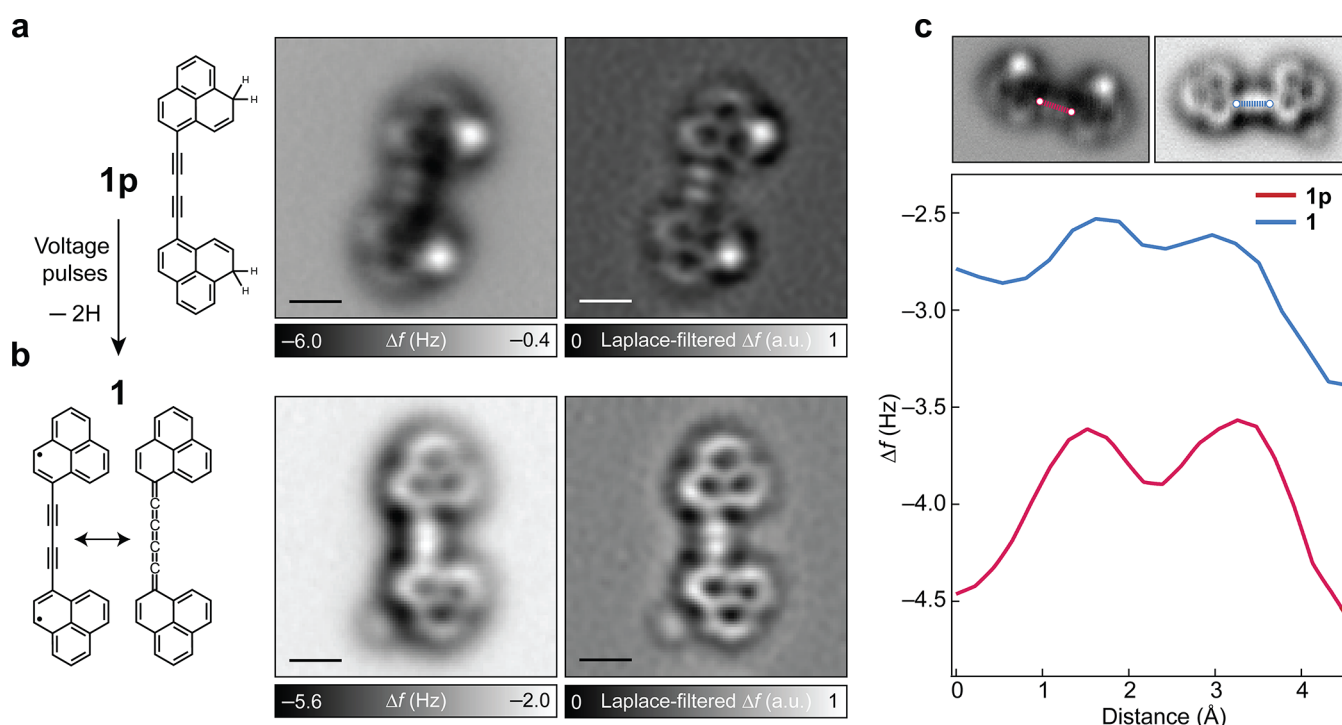


Figure 2. Structural characterization of **1p** and **1**. (a,b) From left to right: chemical structures, AFM images, and corresponding Laplace-filtered AFM images of **1p** (a) and **1** (b); STM set-point: $V = 0.2$ V and $I = 1.0$ pA on NaCl, tip height $\Delta z = 0.5$ Å. a.u. denotes arbitrary units. (c) Δf line profiles along the C_4 chains of **1p** (red) and **1** (blue). Scale bars: 0.5 nm.

Figure 1b for labeling), indicating contribution from the open-shell resonance form. The different bonding motifs for the two resonance structures make **1** a suitable system for characterization by AFM, which can distinguish C–C bonds of different bond orders.³⁰ We show by AFM imaging that compared to a diynic bonding motif with formal C–C single and triple bonds, the C_4 chain in **1** exhibits a markedly reduced bond-order contrast. Furthermore, STM imaging of **1** at the ion resonances reveals orbital densities that cannot be explained on the basis of charge-state transitions involving a single-determinant ground state of **1** (such as a closed-shell configuration with doubly occupied HOMO and empty LUMO). However, the experimental results can be explained well if one considers a ground state of **1** that is composed of multiple Slater determinants, that is, a multiconfigurational ground state.

RESULTS AND DISCUSSION

Generation and Structural Characterization. Compound **1** was generated from the corresponding dihydro precursor **1p** (Figure 2a), which was synthesized in solution (Methods and Figures S1–S8). A submonolayer coverage of **1p** was sublimed on a Cu(111) surface partially covered by bilayer NaCl films (Figure S9). STM and AFM imaging showed the coexistence of both *E* and *Z* configurations of **1p**, which differ in the relative orientation of the two phenalene units through rotation about the C–C single bond connecting the phenalene units and the C_4 chain. AFM imaging (Figures 2 and S10) revealed that both isomers adopt a mostly planar geometry on NaCl, and the *sp*-hybridized C_4 chain exhibits a diynic bonding motif evidenced by a modulation of the frequency shift (Δf) signal along the chain, as described below. Compound **1** was generated by applying voltage pulses to

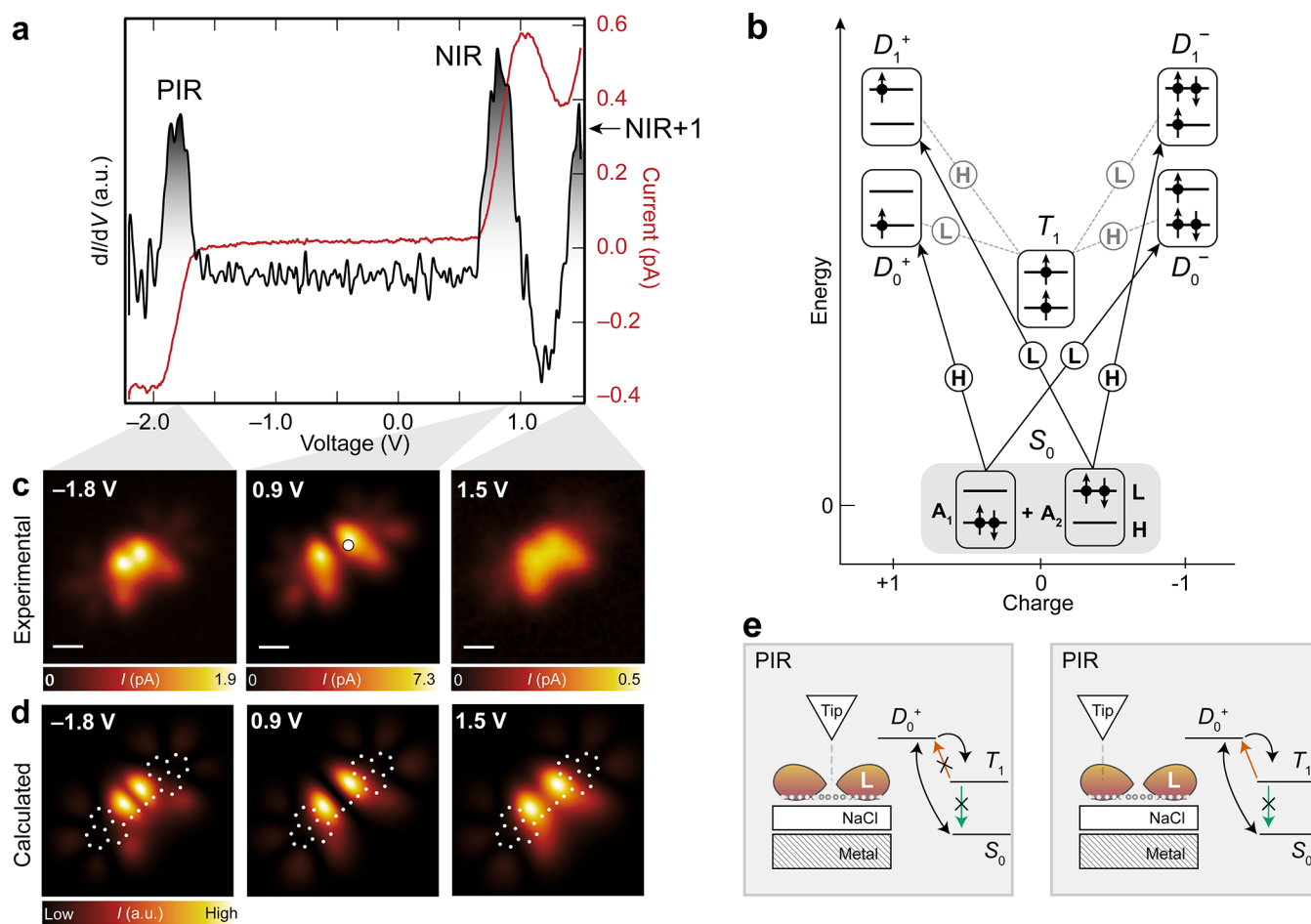


Figure 3. Electronic characterization of **1**. (a) Constant-height $I(V)$ spectrum and the corresponding $dI/dV(V)$ spectrum acquired on **1** (open feedback parameters on the molecule: $V = -2.2$ V, $I = 0.4$ pA). The acquisition position is indicated by the filled white circle in (c). PIR and NIR denote the positive and negative ion resonances, respectively. (b) Scheme of the many-body transitions relevant for the measured ion resonances. The transitions are labeled according to the orbital involved: H (HOMO) or L (LUMO). The $S_0 \rightarrow D_1^+$ transition was not accessible in the experimental voltage range. (c) Constant-height STM images at the ion resonances (from left to right, open feedback parameters on NaCl: $V = -1.8$ V, $I = 1.0$ pA, $\Delta z = 1.9$ Å; $V = 0.9$ V, $I = 1.0$ pA, $\Delta z = 2.3$ Å; $V = 1.5$ V, $I = 1.0$ pA, $\Delta z = 3.5$ Å). (d) Transition probability maps at the voltages corresponding to the experimental images in (c) (see Figures S18, S23, and S24). The molecular structure of **1** is overlaid on the maps. (e) Sketch illustrating triplet trapping for tip positions above the LUMO nodal plane (left), and no trapping for tip positions above finite LUMO density (right). The data in (a,c) were acquired with a metallic tip. Scale bars: 0.5 nm.

individual **1p** molecules by the tip of the STM/AFM system, which led to homolytic cleavage of the two $C(sp^3)-H$ bonds.^{31,32} The sequential manipulation of **1p** to generate **1** was monitored by AFM imaging, with an example shown in Figure S11. In the main text, we focus on the characterization of (*Z*)-**1**. The characterization of (*E*)-**1**, which is electronically and structurally (with respect to the C_4 chain) equivalent to (*Z*)-**1**, is presented in the Supporting Information.

We now focus on elucidating the difference in the bond-order contrasts of the C_4 chain in **1p** and **1**. In AFM imaging, chemical bonds with higher bond orders show a larger Δf signal due to stronger repulsive forces. Figure 2a shows an AFM image of **1p**, where two bright features that correspond to the formal C–C triple bonds^{33,34} labeled b_B in Figure 1b (that exhibit a higher bond order than the neighboring formal C–C single bonds labeled b_A and b_C in Figure 1b) are evident at the center of the C_4 chain. Note that the two bright features at the phenylene units correspond to the dihydro groups. Compared to **1p**, there is a noticeable decrease in the bond-order contrast of the C_4 chain in AFM imaging of **1** (Figure 2b, see also Figures S11 and S12). This difference in the bond-

order contrast is also visualized in the Δf line profiles along the C_4 chains of **1p** and **1** (Figure 2c), where **1p** exhibits a larger Δf modulation compared to **1**. However, the fact that a Δf modulation remains in **1** indicates that the C_4 chain in **1** is neither diyne with formal C–C single and triple bonds (as in **1p**) nor cumulenic (where no bond order contrast should be visible³⁵). We note that changes of the bond order of a molecule have previously been observed due to chemisorption on a metallic surface.³⁶ However, such effects due to interaction with the surface are not expected in our work because of the adsorption of **1** on the inert NaCl surface, where the molecule is physisorbed.

Electronic Characterization. Based on AFM imaging of **1** that reveals bond-order contrast in the C_4 chain that is intermediate between diyne (corresponding to a diradical state with two singly occupied molecular orbitals) and cumulenic (corresponding to a closed-shell state with doubly occupied HOMO and empty LUMO) geometries, and the small DFT-calculated HOMO–LUMO gap of **1** (Figure S13), it is likely that the system exhibits a multiconfigurational ground state. In line with this expectation, STM imaging of **1** at voltages

corresponding to the ion resonances reveals orbital densities that cannot be explained with a single-reference picture but requires invoking a multiconfigurational framework, as discussed below. Here, tunneling events at the ion resonances are considered as many-body transitions between different charge states of **1**, and the electronic ground state of **1** is described by a weighted combination of multiple Slater determinants.

Figure 3a (see also Figures S14–S17) shows a differential conductance spectrum ($dI/dV(V)$, where I and V denote the tunneling current and bias voltage, respectively) acquired on **1**, exhibiting three peaks centered at -1.8 , 0.9 , and 1.5 V, labeled positive ion resonance (PIR), negative ion resonance (NIR), and NIR+1, respectively. In a single-reference picture and assuming a closed-shell electronic configuration, the peak at -1.8 V should correspond to electron detachment from the HOMO of **1**. As shown in Figure S18, the calculated HOMO local density of states (LDOS) map exhibits a maximum at the center of the C_4 chain. Although the STM image at -1.8 V (Figure 3c) shows a high intensity at the center of the C_4 chain, there is a concomitant depression reminiscent of a nodal plane, which is not explained by a transition involving only the HOMO. At positive biases, the resonance at 0.9 V should correspond to electron attachment to the LUMO of **1**, and in this case, the LUMO LDOS map (Figure S18) agrees well with the STM image at 0.9 V. However, for the resonance at 1.5 V, which should correspond to electron attachment to the LUMO+1 of the molecule, the corresponding STM image should show the superposition of LUMO and LUMO+1 densities (because electron attachment to both LUMO and LUMO+1 is possible at this bias). The STM image at 1.5 V does not agree well with the LDOS map corresponding to the superposition of the LUMO and LUMO+1 (Figure S18), but counter-intuitively, agrees better with the LDOS map corresponding to the superposition of the HOMO and LUMO. Clearly, a single-reference picture fails to account for these peculiar features in the STM images.

The experimental STM images can be reconciled with measured orbital densities if one instead considers a multiconfigurational picture, as demonstrated previously for a similar case.³⁷ Within a minimal multiconfigurational framework, the neutral singlet ground state of **1** (S_0) is described as a linear combination of two Slater determinants ψ_B and ψ_{AB}

$$S_0 = A_1\psi_B + A_2\psi_{AB} \quad (1)$$

where $\psi_B = |\uparrow\downarrow\rangle_{\text{HOMO}}|0\rangle_{\text{LUMO}}$ and $\psi_{AB} = |0\rangle_{\text{HOMO}}|\uparrow\downarrow\rangle_{\text{LUMO}}$ correspond to electronic configurations with bonding (doubly occupied HOMO and empty LUMO) and antibonding (empty HOMO and doubly occupied LUMO) symmetries, respectively. To validate our assumption about the multiconfigurational ground state of **1** (eq 1), we performed calculations using the density matrix renormalization group (DMRG) for the Hubbard model as well as complete active space self-consistent field (Methods, Figures S13 and S19–S23, and Tables S1–S4). All calculations were done for three distinct geometries of **1**: a DFT PBE0-XC UKS optimized structure, a cumulenic structure with all double bonds (from PBE0 optimized ethylene) in the C_4 chain, and a diyenic structure with alternating single and triple bonds (from PBE0 optimized propyne) in the C_4 chain (Tables S5–S7). For brevity, we will focus on the DMRG results, yielding the most accurate description³⁸ of the multiconfigurational nature of **1**. The calculations corroborate the assumption of a singlet ground

state with a predominantly bonding character ($|A_1|^2/|A_2|^2 > 4$) across all considered geometries. The weight of the doubly excited configuration, $|A_2|^2$, ranges from 0.04 to 0.12, increasing from the cumulenic to the diyenic structure. For the DFT PBE0-XC UKS optimized structure, which is the focus of the following analysis, we obtain $|A_1|^2 = 0.60$ and $|A_2|^2 = 0.06$. Since $|A_1|^2 + |A_2|^2 < 1$, the ground state S_0 involves more Slater determinants than suggested by the simplified picture of eq 1. However, as we show, this two-configuration picture describes well the observed electronic properties of **1**.

Figure 3b illustrates a schematic of the many-body electronic transitions corresponding to the measured ion resonances of **1**. To elucidate the excitation mechanisms responsible for the experimental STM images in Figure 3c, we modeled the system using a master equation (Methods and Figure S24 and Table S4) that incorporates all relevant tunneling pathways and a finite lifetime of the neutral excited states. The spatially resolved transition probability maps (Figure 3d) associated with the transitions depicted in Figure 3b were derived from Dyson orbitals computed via DMRG (Figures S18 and S22–S24). For this, we assumed tunneling with an s-wave tip because of the predominant s-wave tunneling character at large tip–sample distances, even for carbon monoxide-functionalized tips.³⁹ Starting from S_0 , we assign the positive ion resonance at -1.8 V to a resonant transition to the cationic doublet ground state D_0^+ , wherein an electron is detached from the HOMO. The system subsequently decays to S_0 by electron transfer from the surface, resulting in a net current. However, the corresponding $S_0 \rightarrow D_0^+$ Dyson orbital (Figures S22 and S23) does not feature a central nodal plane, as observed in the STM image at -1.8 V. To resolve this discrepancy, one must consider the role of the neutral triplet excited state T_1 . Following an initial $S_0 \rightarrow D_0^+$ resonant tunneling event, the system can be neutralized via electron transfer from the surface in two different ways. By electron attachment to the HOMO, the system decays to S_0 , while by electron attachment to the LUMO, the system decays to T_1 (located ~ 0.36 eV above S_0 according to DMRG calculations). If the system is in T_1 , it can either decay to S_0 (which is a slow process because it requires a change in the spin multiplicity), or the system can be excited to D_0^+ via electron tunneling to the tip, followed by a decay to S_0 . As shown schematically in Figure 3e, the amplitude of the $T_1 \rightarrow D_0^+$ transition, which involves electron detachment from the LUMO, is strongly dependent on the tip position. If the tip is located at the center of the C_4 chain (where the LUMO exhibits a nodal plane), the system is trapped in T_1 . The tunneling channel through the molecule is effectively blocked, and the total current is reduced at the nodal plane, as observed in the STM image. Away from the chain center, where the LUMO has a nonzero amplitude, this transition can take place. The corresponding transition probability map, which takes into account the $S_0 \rightarrow D_0^+$ and $T_1 \rightarrow D_0^+$ transitions (Figure 3d, see also Figure S23 for the relative intensities of the transitions), exhibits good agreement with the STM image at -1.8 V. We note that transitions involving ground and excited states of a molecule have been previously predicted for copper phthalocyanine,⁴⁰ and experimentally observed for several molecular systems by STM/AFM-based spectroscopy^{37,41–43} and STM-induced luminescence measurements.^{44,45}

The NIR at 0.9 V represents a resonant transition from S_0 to the anionic doublet ground state D_0^- , corresponding to electron attachment to the LUMO. The Dyson orbital for this transition features the characteristic central nodal plane as

seen in the experiment. The system may subsequently decay to either S_0 or T_1 , as described above. The decay to T_1 opens an additional tunneling channel via the $T_1 \rightarrow D_0^-$ transition, which does not feature a central nodal plane (as it involves electron attachment to the HOMO). However, this pathway does not alter the appearance of the STM image because if the tip is positioned above the nodal plane of the $S_0 \rightarrow D_0^-$ transition, the system is not excited to D_0^- and, therefore, cannot decay to T_1 . The transition probability map that takes into account the $S_0 \rightarrow D_0^-$ and $T_1 \rightarrow D_0^-$ transitions reproduces the experimental STM image at 0.9 V. The NIR+1 at 1.5 V corresponds to a resonant transition from S_0 to the anionic doublet excited state D_1^- , where an electron is attached to the HOMO. This process becomes possible because of the multiconfigurational ground state of **1**, where the ψ_{AB} component of S_0 contributes. The transition probability map, which, besides the resonant $S_0 \rightarrow D_1^-$ transition, includes contributions from the off-resonant $S_0 \rightarrow D_0^-$ transition (accessible at 1.5 V but with reduced spectral weight), and the $T_1 \rightarrow D_0^-$ and $T_1 \rightarrow D_1^-$ transitions, exhibits good agreement with the experimental STM image at 1.5 V.

The explanations for the effects of the multiconfigurational ground state on STM orbital density images were brought forward by Yu et al.³⁷ Here, in addition to the STM orbital density images, we also observe signatures of the multiconfigurational ground state of a molecule by AFM, revealing contributions from both cumulenic and diynic resonance structures.

CONCLUSIONS

We presented the generation and characterization of a neutral diradicaloid **1**, revealing experimental signatures and observables related to its multiconfigurational ground state in scanning probe measurements. We showed that the maps of charge-state transitions of **1** measured by STM cannot be explained by a picture wherein electron detachment or attachment takes place in the framework of single-particle states, but can only be explained if the ground state of **1** is considered to be a multiconfigurational state consisting of a weighted combination of multiple Slater determinants. Moreover, and in line with the observations of the STM measurements, AFM imaging reveals that the C_4 bridge of **1** exhibits a bond-order contrast that is intermediate between diynic and cumulenic bonding motifs, lending support to the picture that **1** is neither a diradical nor a closed-shell system but a diradicaloid best described as a resonance hybrid of open- and closed-shell states. Our study thus provides a striking example of strong electronic correlations manifesting at the atomic scale in real space.

ASSOCIATED CONTENT

Data Availability Statement

The raw NMR data are available free of charge on the public repository Zenodo under the link: <https://zenodo.org/record/15311165> (DOI: 10.5281/zenodo.15311165).

Supporting Information

The Supporting Information is available free of charge at <https://pubs.acs.org/doi/10.1021/jacs.5c13039>.

Experimental and theoretical methods, additional scanning probe and theoretical data, atomic coordinates of the three geometries of **1**, and solution synthesis and characterization (PDF)

AUTHOR INFORMATION

Corresponding Authors

Elia Turco – *nanotech@surfaces Laboratory, Empa—Swiss Federal Laboratories for Materials Science and Technology, 8600 Dübendorf, Switzerland*; Present Address: *QuTech and Kavli Institute of Nanoscience, Delft University of Technology, 2600 GA Delft, The Netherlands*; orcid.org/0000-0002-6437-9334; Email: e.turco@tudelft.nl

Shantanu Mishra – *IBM Research Europe—Zurich, 8803 Rüschlikon, Switzerland*; *Department of Physics, Chalmers University of Technology, 412 96 Gothenburg, Sweden*; orcid.org/0000-0002-2900-4203; Email: shantanu.mishra@chalmers.se

Authors

Lara Tejerina – *Department of Chemistry, University of Zurich, 8057 Zurich, Switzerland*; orcid.org/0000-0003-1000-6310

Gonçalo Catarina – *nanotech@surfaces Laboratory, Empa—Swiss Federal Laboratories for Materials Science and Technology, 8600 Dübendorf, Switzerland*; orcid.org/0000-0002-7341-0495

Andres Ortega-Guerrero – *nanotech@surfaces Laboratory, Empa—Swiss Federal Laboratories for Materials Science and Technology, 8600 Dübendorf, Switzerland*

Nils Krane – *nanotech@surfaces Laboratory, Empa—Swiss Federal Laboratories for Materials Science and Technology, 8600 Dübendorf, Switzerland*; orcid.org/0009-0004-6970-0846

Leo Gross – *IBM Research Europe—Zurich, 8803 Rüschlikon, Switzerland*; orcid.org/0000-0002-5337-4159

Michal Juríček – *Department of Chemistry, University of Zurich, 8057 Zurich, Switzerland*; orcid.org/0000-0001-5595-431X

Complete contact information is available at: <https://pubs.acs.org/10.1021/jacs.5c13039>

Author Contributions

[#]L.T. and G.C. contributed equally to this work.

Notes

The authors declare no competing financial interest.

ACKNOWLEDGMENTS

E.T. would like to thank Carlo Antonio Pignedoli and Aliaksandr Yakutovich for fruitful discussions. This research was financially supported by the H2020-MSCA-ITN (ULTIMATE, no. 813036); the Swiss National Science Foundation (grant nos. CRSII5_205987 (PiMag), 212875, PP00P2_170534, and TMC2-2_213829/CASCADER); the Werner Siemens Foundation (CarboQuant); and the European Research Council Synergy Grant MolDAM (grant no. 951519). A.O.-G. and G.C. acknowledge financial support from the NCCR MARVEL, a National Centre of Competence in Research funded by the Swiss National Science Foundation (grant no. 205602). L.T. and M.J. also acknowledge the Dr. Helmut Legerlotz Foundation (University of Zurich).

REFERENCES

- (1) Stuyver, T.; Chen, B.; Zeng, T.; Geerlings, P.; De Proft, F.; Hoffmann, R. Do Diradicals Behave Like Radicals? *Chem. Rev.* **2019**, *119*, 11291–11351.
- (2) Abe, M. Diradicals. *Chem. Rev.* **2013**, *113*, 7011–7088.
- (3) Wu, J., Ed.; *Diradicaloids*; Jenny Stanford Publishing: New York, 2022.
- (4) Nakano, M.; Fukui, H.; Minami, T.; Yoneda, K.; Shigeta, Y.; Kishi, R.; Champagne, B.; Botek, E.; Kubo, T.; Ohta, K.; Kamada, K. (Hyper)polarizability density analysis for open-shell molecular systems based on natural orbitals and occupation numbers. *Theor. Chem. Acc.* **2011**, *130*, 711–724.
- (5) Gryn'ova, G.; Coote, M. L.; Corminboeuf, C. Theory and practice of uncommon molecular electronic configurations. *Wiley Interdiscip. Rev.: Comput. Mol. Sci.* **2015**, *5*, 440–459.
- (6) Y Gopalakrishna, T.; Zeng, W.; Lu, X.; Wu, J. From open-shell singlet diradicaloids to polyradicaloids. *Chem. Commun.* **2018**, *54*, 2186–2199.
- (7) Zuzak, R.; Kumar, M.; Stoica, O.; Soler-Polo, D.; Brabec, J.; Pernal, K.; Veis, L.; Blicek, R.; Echavarren, A. M.; Jelinek, P.; Godlewski, S. On-Surface Synthesis and Determination of the Open-Shell Singlet Ground State of Tridecacene. *Angew. Chem., Int. Ed.* **2024**, *63*, No. e202317091.
- (8) Ruan, Z.; Schramm, J.; Bauer, J. B.; Naumann, T.; Müller, L. V.; Sättele, F.; Bettinger, H. F.; Tonner-Zech, R.; Gottfried, J. M. On-Surface Synthesis and Characterization of Pentadecacene and Its Gold Complexes. *J. Am. Chem. Soc.* **2025**, *147*, 4862–4870.
- (9) Hayashi, H.; Yamada, H. Exploring the chemistry of higher acenes: from synthesis to applications. *Chem. Sci.* **2025**, *16*, 11204–11231.
- (10) Sánchez-Grande, A.; Urgel, J. I.; Veis, L.; Edalatmanesh, S.; Santos, J.; Lauwaet, K.; Mutombo, P.; Gallego, J. M.; Brabec, J.; Beran, P.; Nachtigallová, D.; Miranda, R.; Martín, N.; Jelínek, P.; Ěcija, D. Unravelling the Open-Shell Character of Peripentacene on Au(111). *J. Phys. Chem. Lett.* **2021**, *12*, 330–336.
- (11) Konishi, A.; Hirao, Y.; Nakano, M.; Shimizu, A.; Botek, E.; Champagne, B.; Shiomi, D.; Sato, K.; Takui, T.; Matsumoto, K.; Kurata, H.; Kubo, T. Synthesis and Characterization of Teranthene: A Singlet Biradical Polycyclic Aromatic Hydrocarbon Having Kekulé Structures. *J. Am. Chem. Soc.* **2010**, *132*, 11021–11023.
- (12) Konishi, A.; Hirao, Y.; Matsumoto, K.; Kurata, H.; Kishi, R.; Shigeta, Y.; Nakano, M.; Tokunaga, K.; Kamada, K.; Kubo, T. Synthesis and Characterization of Quarteranthene: Elucidating the Characteristics of the Edge State of Graphene Nanoribbons at the Molecular Level. *J. Am. Chem. Soc.* **2013**, *135*, 1430–1437.
- (13) Wang, S.; Talirz, L.; Pignedoli, C. A.; Feng, X.; Müllen, K.; Fasel, R.; Ruffieux, P. Giant edge state splitting at atomically precise graphene zigzag edges. *Nat. Commun.* **2016**, *7*, 11507.
- (14) Huang, R.; Phan, H.; Herng, T. S.; Hu, P.; Zeng, W.; Dong, S.-q.; Das, S.; Shen, Y.; Ding, J.; Casanova, D.; Wu, J. Higher Order π -Conjugated Polycyclic Hydrocarbons with Open-Shell Singlet Ground State: Nonazethrene versus Nonacene. *J. Am. Chem. Soc.* **2016**, *138*, 10323–10330.
- (15) Zeng, W.; Sun, Z.; Herng, T. S.; Gonçalves, T. P.; Gopalakrishna, T. Y.; Huang, K.-W.; Ding, J.; Wu, J. Superheptazethrene. *Angew. Chem., Int. Ed.* **2016**, *55*, 8615–8619.
- (16) Hu, P.; Wu, J. Modern zethrene chemistry. *Can. J. Chem.* **2017**, *95*, 223–233.
- (17) Zeng, W.; Gopalakrishna, T. Y.; Phan, H.; Tanaka, T.; Herng, T. S.; Ding, J.; Osuka, A.; Wu, J. Superoctazethrene: An Open-Shell Graphene-like Molecule Possessing Large Diradical Character but Still with Reasonable Stability. *J. Am. Chem. Soc.* **2018**, *140*, 14054–14058.
- (18) Turco, E.; Mishra, S.; Melidonie, J.; Eimre, K.; Obermann, S.; Pignedoli, C. A.; Fasel, R.; Feng, X.; Ruffieux, P. On-Surface Synthesis and Characterization of Super-nonazethrene. *J. Phys. Chem. Lett.* **2021**, *12*, 8314–8319.
- (19) Mishra, S.; Melidonie, J.; Eimre, K.; Obermann, S.; Gröning, O.; Pignedoli, C. A.; Ruffieux, P.; Feng, X.; Fasel, R. On-surface synthesis of super-heptazethrene. *Chem. Commun.* **2020**, *56*, 7467–7470.
- (20) Mishra, S.; Yao, X.; Chen, Q.; Eimre, K.; Gröning, O.; Ortiz, R.; Di Giovannantonio, M.; Sancho-García, J. C.; Fernández-Rossier, J.; Pignedoli, C. A.; Müllen, K.; Ruffieux, P.; Narita, A.; Fasel, R. Large magnetic exchange coupling in rhombus-shaped nanographenes with zigzag periphery. *Nat. Chem.* **2021**, *13*, 581–586.
- (21) Biswas, K.; et al. Steering Large Magnetic Exchange Coupling in Nanographenes near the Closed-Shell to Open-Shell Transition. *J. Am. Chem. Soc.* **2023**, *145*, 2968–2974.
- (22) Shimizu, A.; Kishi, R.; Nakano, M.; Shiomi, D.; Sato, K.; Takui, T.; Hisaki, I.; Miyata, M.; Tobe, Y. Indeno[2,1-*b*]fluorene: A 20- π -Electron Hydrocarbon with Very Low-Energy Light Absorption. *Angew. Chem., Int. Ed.* **2013**, *52*, 6076–6079.
- (23) Dressler, J. J.; Zhou, Z.; Marshall, J. L.; Kishi, R.; Takamuku, S.; Wei, Z.; Spisak, S. N.; Nakano, M.; Petrukchina, M. A.; Haley, M. M. Synthesis of the Unknown Indeno[1,2-*a*]fluorene Regioisomer: Crystallographic Characterization of Its Dianion. *Angew. Chem., Int. Ed.* **2017**, *56*, 15363–15367.
- (24) Di Giovannantonio, M.; Eimre, K.; Yakutovich, A. V.; Chen, Q.; Mishra, S.; Urgel, J. I.; Pignedoli, C. A.; Ruffieux, P.; Müllen, K.; Narita, A.; Fasel, R. On-Surface Synthesis of Antiaromatic and Open-Shell Indeno[2,1-*b*]fluorene Polymers and Their Lateral Fusion into Porous Ribbons. *J. Am. Chem. Soc.* **2019**, *141*, 12346–12354.
- (25) Mishra, S.; Vilas-Varela, M.; Lieske, L.-A.; Ortiz, R.; Fatayer, S.; Rončević, I.; Albrecht, F.; Frederiksen, T.; Peña, D.; Gross, L. Bistability between π -diradical open-shell and closed-shell states in indeno[1,2-*a*]fluorene. *Nat. Chem.* **2024**, *16*, 755–761.
- (26) Clair, S.; de Oteyza, D. G. Controlling a Chemical Coupling Reaction on a Surface: Tools and Strategies for On-Surface Synthesis. *Chem. Rev.* **2019**, *119*, 4717–4776.
- (27) Ovchinnikov, A. A. Multiplicity of the ground state of large alternant organic molecules with conjugated bonds. *Theor. Chim. Acta* **1978**, *47*, 297–304.
- (28) Lieb, E. H. Two theorems on the Hubbard model. *Phys. Rev. Lett.* **1989**, *62*, 1201–1204.
- (29) Hirao, Y.; Daifuku, Y.; Ihara, K.; Kubo, T. Spin–Spin Interactions in One-Dimensional Assemblies of a Cumulene-Based Singlet Biradical. *Angew. Chem., Int. Ed.* **2021**, *60*, 21319–21326.
- (30) Gross, L.; Mohn, F.; Moll, N.; Schuler, B.; Criado, A.; Guitián, E.; Peña, D.; Gourdon, A.; Meyer, G. Bond-Order Discrimination by Atomic Force Microscopy. *Science* **2012**, *337*, 1326–1329.
- (31) Turco, E.; Bernhardt, A.; Krane, N.; Valenta, L.; Fasel, R.; Juriček, M.; Ruffieux, P. Observation of the Magnetic Ground State of the Two Smallest Triangular Nanographenes. *JACS Au* **2023**, *3*, 1358–1364.
- (32) Pavliček, N.; Mistry, A.; Majzik, Z.; Moll, N.; Meyer, G.; Fox, D. J.; Gross, L. Synthesis and characterization of triangulene. *Nat. Nanotechnol.* **2017**, *12*, 308–311.
- (33) de Oteyza, D. G.; Gorman, P.; Chen, Y.-C.; Wickenburg, S.; Riss, A.; Mowbray, D. J.; Etkin, G.; Pedramrazi, Z.; Tsai, H.-Z.; Rubio, A.; Crommie, M. F.; Fischer, F. R. Direct Imaging of Covalent Bond Structure in Single-Molecule Chemical Reactions. *Science* **2013**, *340*, 1434–1437.
- (34) Pavliček, N.; Gawel, P.; Kohn, D. R.; Majzik, Z.; Xiong, Y.; Meyer, G.; Anderson, H. L.; Gross, L. Polyyne formation via skeletal rearrangement induced by atomic manipulation. *Nat. Chem.* **2018**, *10*, 853–858.
- (35) Sun, L.; Zheng, W.; Gao, W.; Kang, F.; Zhao, M.; Xu, W. On-surface synthesis of aromatic cyclo[10]carbon and cyclo[14]carbon. *Nature* **2023**, *623*, 972–976.
- (36) Majzik, Z.; Pavliček, N.; Vilas-Varela, M.; Pérez, D.; Moll, N.; Guitián, E.; Meyer, G.; Peña, D.; Gross, L. Studying an antiaromatic polycyclic hydrocarbon adsorbed on different surfaces. *Nat. Commun.* **2018**, *9*, 1198.
- (37) Yu, P.; Kocić, N.; Repp, J.; Siegert, B.; Donarini, A. Apparent Reversal of Molecular Orbitals Reveals Entanglement. *Phys. Rev. Lett.* **2017**, *119*, 056801.

(38) Catarina, G.; Turco, E.; Krane, N.; Bommert, M.; Ortega-Guerrero, A.; Gröning, O.; Ruffieux, P.; Fasel, R.; Pignedoli, C. A. Conformational Tuning of Magnetic Interactions in Coupled Nanographenes. *Nano Lett.* **2024**, *24*, 12536–12544.

(39) Paschke, F.; Lieske, L.-A.; Albrecht, F.; Chen, C. J.; Repp, J.; Gross, L. Distance and Voltage Dependence of Orbital Density Imaging Using a CO-Functionalized Tip in Scanning Tunneling Microscopy. *ACS Nano* **2025**, *19*, 2641–2650.

(40) Siegert, B.; Donarini, A.; Grifoni, M. Nonequilibrium spin crossover in copper phthalocyanine. *Phys. Rev. B* **2016**, *93*, 121406.

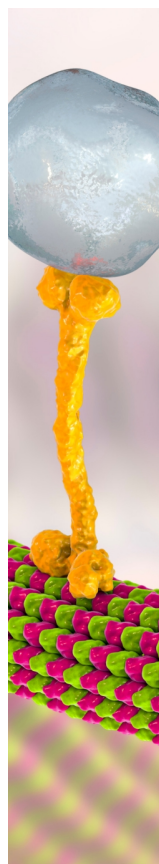
(41) Fatayer, S.; Albrecht, F.; Tavernelli, I.; Persson, M.; Moll, N.; Gross, L. Probing Molecular Excited States by Atomic Force Microscopy. *Phys. Rev. Lett.* **2021**, *126*, 176801.

(42) Peng, J.; Sokolov, S.; Hernangómez-Pérez, D.; Evers, F.; Gross, L.; Lupton, J. M.; Repp, J. Atomically resolved single-molecule triplet quenching. *Science* **2021**, *373*, 452–456.

(43) Sellies, L.; Eckrich, J.; Gross, L.; Donarini, A.; Repp, J. Controlled single-electron transfer enables time-resolved excited-state spectroscopy of individual molecules. *Nat. Nanotechnol.* **2025**, *20*, 27–35.

(44) Jiang, S.; Neuman, T.; Bretel, R.; Boeglin, A.; Scheurer, F.; Le Moal, E.; Schull, G. Many-Body Description of STM-Induced Fluorescence of Charged Molecules. *Phys. Rev. Lett.* **2023**, *130*, 126202.

(45) Hung, T.-C.; Robles, R.; Kiraly, B.; Strik, J. H.; Rutten, B. A.; Khajetoorians, A. A.; Lorente, N.; Wegner, D. Bipolar single-molecule electroluminescence and electrofluorochromism. *Phys. Rev. Res.* **2023**, *5*, 033027.



CAS BIOFINDER DISCOVERY PLATFORM™

BRIDGE BIOLOGY AND CHEMISTRY FOR FASTER ANSWERS

Analyze target relationships,
compound effects, and disease
pathways

Explore the platform

